European Journal of Chemistry

Highly active mesoporous SiO₂-TiO₂ based nanocomposites for photocatalytic degradation of textile dyes and phenol

Asima Siddiqa [a],*, Sumbul Sabir [b], Syed Tajammul Hussain [a] and Bakhtiar Muhammad [b]

[a] National Centre for Physics, Quaid-i-Azam University Complex, Islamabad, 44000, Pakistan
[b] Chemistry Department, Hazara University, Mansehra, 21120, Pakistan

*Corresponding author at: National Centre for Physics, Quaid-i-Azam University Complex, Islamabad, 44000, Pakistan.
Tel.: +92.51.2077480; fax: +92.51.2077395. E-mail address: a.sam.malik@gmail.com (A. Siddiqa).

ARTICLE INFORMATION

ABSTRACT

Titania-silica nanocomposites (20% SiO_2-TiO_2, 30% SiO_2-TiO_2, 40% SiO_2-TiO_2 and 50 % SiO_2-TiO_2) with tailored morphology and tunable band energy have been synthesized successfully via micro emulsion method. The morphology, chemical composition, band gap energy and stability of prepared nanocomposites were investigated by XRD, SEM/EDX, FT-IR, DRS and TGA. While textural parameters such as surface area, pore volume, and pore diameter were evaluated by nitrogen adsorption-desorption isotherms. The prepared nanocomposites were employed for photocatalytic degradation of phenol and dyes (methyl yellow, auramine O, turquoise blue G) under visible light irradiations. The results of photocatalytic degradation and kinetic parameter (K_{app}) strongly suggest that 20% SiO_2-TiO_2 showed remarkable photocatalytic efficiency in comparison to SiO_2-TiO_2 nanocomposites with high silica contents. These findings proved significantly that 20% SiO_2-TiO_2 have marked impact on the photocatalytic efficiency due to its high pore volume, more diameter, high availability of anatase TiO_2 in nanocomposite and reduced bandgap energy.

1. Introduction

Water is one of the most important commodities, covering about 70% of earth. Considerable volumes of water are required for drinking, domestic purposes, agriculture and industry [1,2]. Approximately, 200 L of water per day is used for agriculture purposes; 300-400 L of water is required for domestic, drinking purposes and for industrial usage 250,000 L of water is needed [3]. And, on the whole, experts warn that total water demand will increase immensely in the world this century. For industry water supply it will triple, for public it will double and for agriculture it will increase by 1.5 times [4,5]. There is an increasing concern for rapidly diminishing supply of water because of sudden increased demand for fresh water due to increasing population growth and exploitation of industry and agriculture [6,7]. There is threat that by the end of this century water will become a dominating world problem. The most pressing issues badly affecting human being through out the world is insufficient access to clean, abundant fresh water [3-5]. One of the main causes for the water crisis is water contamination. On average, two million tons of human excrement as well as toxic industrial wastes are carelessly dumped daily and thus polluting rivers, soil and oceans [7,8]. Industrial effluents including phenols, chlorophenols, oils and organic dyes, disposed off from the fabric, paint, tannery and food industries, constitute one of the major sources of water pollution [9]. However, ubiquitous industrial dyes are one of the major notorious pollutants due to; their huge production from industries, decoloration, slow biodegradability and toxicity [10,11]. Approximately, 700,000 tons of dyes are produced annually and nearly 1-20% of the total world production is discharged in textile effluents [8,9]. Moreover, byproducts of some dyes including azo dyes, fluorinated dyes

are extremely toxic, carcinogenic and mutagenic because of their high stability and resistance to degradation [12]. However, the removal of these toxic textile dyes from aquatic environment has become a major focus of research. Numerous commercial, domestic and industrially developed water purification techniques comprising oxidation, membrane filtration, chemical coagulation or flocculation combined with flotation and filtration processes have been adopted previously to deal with contaminated water [11,13,14]. Unfortunately, the requirements of water purification cannot be met by these conventional methods due to expensiveness, addition of huge number of refractory materials in water discharge, complexity in complete removal of color [15]. Worldwide, numerous catalytic technologies have been adopted extensively for complete removal of dyes from waste water [16,17]. These include photocatalytic oxidation, activated carbon adsorption, photoelectrocatalytic adsorption, coupled semiconductors, thin-films based photocatalytic degradation, fenton and photofenton catalytic reactions, microwave and UV eliminated processes [15-18]. Among these approaches, photocatalytic degradation using heterogeneous metal oxide semiconductors have accomplished significant attention during the last few decades due to its cost effectiveness, extraordinary oxidative stability and complete removal of contaminants leading to complete mineralization [19]. Up to now, several metal oxides including zinc oxide (ZnO), titanium oxide (TiO_2), tungstate (WO_3), cadmium sulphide (Cds), vanadate (VO_4) and others have been reported for photocatalytic degradation of contaminants in aqueous media [19-21]. Among them, titania (TiO_2) has gained much interest regarding its application as a photocatalyst for degradation of industrial organic pollutants from contaminated water due to its outstanding properties such as low cost, high oxidative power of generating holes and

long term photochemical stability and confined porous structure [22]. However, some limitations such as wide band gap, low optical absorptions and fast electron-hole pair recombination rate are associated with TiO_2 [20,22]. Several strategies have been adopted to overcome these drawbacks including metal doping with Au, Ru, Cu, Ag and Fe; semiconductor coupling with SiO_2, $Al2O_3$, SnO_2, ZnO and WO_3; and creation of oxygen vacancies [20-22]. Among them, titania-silica nanocomposites exhibit high thermal stability, surface area and better photocatalytic activity than pure TiO_2 [23]. Such materials are regarded as a potential candidate as photocatalyst. The most extensively used chemical processes to synthesize silica-titania composite nanoparticles include sol gel processing, co-precipitation, high energy milling, plasma or flame spraying synthesis, flash combustion technique and micellar micro emulsion method [24-26]. The micro emulsion method is found to be facile rout for synthesis of SiO_2-TiO_2 nanocomposites with relatively high thermal stability of titania, increased surface area, enhanced photocatalytic activity [25,26]. However, little literature is available on the removal of industrial organic pollutants from contaminated water using SiO_2-TiO_2 based nanocomposite. Ali Mahyar *et al.* reported the TiO_2/SiO_2 composite as a photo catalyst for the degradation of C.I. Basic Voilet 2 [27]. H. Chun et al prepared TiO_2-SiO_2 nanocomposite for the decolorization of dyes including cationic dyes, cationic blue X-GRL (CBX) and cationic pink FG (FG), and anionic reactive brilliant red K-2G (K-2G), reactive yellow KD-3G (KD-3G), and acid red B (ARB) under UV illumination [28]. J.W. Lee *et al.* investigated decomposition of azo dyes using the SiO_2-TiO_2 core-shell particles [29]. In of the study, Zhe-Ying Shen *et al.*, used h+-SiO_2-TiO_2 microspheres for the degradation of methyl orange in water under UV light irradiation [30].

In the present work, we have synthesized mesoporous SiO_2-TiO_2 nanocomposites with varying SiO_2 contents using inverse microemulsion method. The prepared material showed high surface area, high thermal stability and enhanced photocatalytic activity for the degradation of phenol and dyes (Auramine O, Methyl Yellow and Turquoise Blue G) under visible light. Furthermore, the effects of varying silica content on the phase transformation of titania, optical properties, surface area, photocatalytic activity and kinetic parameters were studied also for comparison. The data obtained significantly suggests the improvement not only in the synthesis method but also in its industrial applications for removal of textile dyes from the contaminate water which will help to open new directions in this very important area.

2. Experimental

2.1. Materials

Titanium tetraisopropoxide [Ti $(OC_3H_7)_4$, TTIP] 98.0% and tetra ethyl ortho silicate [$C_8H_{20}O_4Si$, TEOS] 99% were purchased from Merck. Ammonium hydroxide (NH_4OH) 33%, toluene ($C_6H_5CH_3$) 96%, benzyl alcohol (C_7H_8O) 99% and Triton X-100 (*t*-Oct-C_6H_4-(OCH_2CH_2)$_x$OH, x = 9-10) 98% were obtained from Merck. Auramine O ($C_{17}H_{21}N_3$) 85%, methyl yellow ($C_{14}H_{15}N_3$) 85%, Turquoise blue G ($C_{42}H_{25}N_7Na_4O_{13}S_4$) 98%, phenol ($C_6H_5OH$) 99.5% were purchased from Fluka.

2.2. Preparation of nanocomposite

SiO_2-TiO_2 nanocomposites with different silica weight percents (20 wt %, 30 wt %, 40 wt % and 50 wt % of TiO_2) were synthesized via micro emulsion method. The first step in synthesis of micro emulsion involves mixing a required amount of toluene, water and benzyl alcohol (7:5:1, *v:v:v*). In the second step Triton X-100 (7 mL) was added drop wise into the above suspension until solution became transparent.

In the micro emulsion mixture, desired amount of tetra ethyl ortho silicate was injected followed by drop wise addition of

ammonia hydroxide under vigorous stirring till pH reached 10. Then desired amount of TTIP was added in above mixture, stirred for 12 hrs until it became milky white. This suspension was centrifuged at 4000 rpm for 20 min, washed with deionized water and anhydrous ethanol in order to remove the organic contaminations and surfactant. The resulting sample was dried in vacuum oven at 105 °C and calcined for 4 hrs at 550 °C to get the final product.

2.3. Characterization

The structural parameters like crystallanity, phase and crystallite size of powder samples was determined by Powder XRD using a Phillips PW 3040/60 X Pert Pro powder diffractometer with Cu Kα radiation of wavelength of 1.5406 Å in the 2θ range of 15 to 75° with a step size of 0.05 ° and step time of 3 s. The morphology and elemental composition of the obtained catalyst were observed using SEM, equipped with an energy-dispersive spectrometer EDX (LEO 1530 FEG-SEM-EDX). FT-IR spectra were recorded on Nicolet 6700 FT-IR spectrometer to evaluate the chemical structure of prepared materials. Specific surface area (BET) was determined by Nitrogen adsorption-desorption isotherms recorded at liquid nitrogen temperature (77K) on a Quantachrome Instrument (NOVA 1000 series). The average pore volume and pore size distribution was derived from Barrett-Joyner-Halenda (BJH) desorption isotherms. Thermal gravimetric analysis was performed on TG-TDA (Perkin-Elmer) from 25 to 1200 °C at constant rate of 5-10 °C/min to examine possible decom-position and phase change temperature. The diffuse reflectance spectroscopy (DRS) was carried out to evaluate optical properties of samples. Band gap energies of catalyst were calculated by using Munk's function [$F(R)^2$]. RBS analysis was carried out for detailed composition and metal oxide distribution in the synthesized samples. A collimated 2.0 MeV He+ beam produced by 5UDH-2 Pelletron was used for RBS channeling measurements. The sample was mounted on a high precision (0.01 °) five-axis goniometer in a vacuum chamber, so that the orientation of this sample relative to the He+ beam could be precisely controlled. The backscattered particles were collected by Silicon Surface Barrier (SSB) detector (FWHM 11 KeV and area 50 mm²) using energy resolution of 25 KeV placed at angle of 170 °. UV-Vis Spectroscopic analysis in the range 200-800 nm was performed on Shimadzu UV-1700 spectrophotometer in order to measure the absorbance of samples.

2.4. Photocatalytic activity measurements

The detailed experimental setup used to study the removal of industrial dyes from water under solar radiation is described in detail in our previous publication [31]. The photocatalytic activities of prepared nanocomposites were evaluated by photocatalytic degradation of aqueous solutions of organic pollutants (methyl yellow, auramine O, turquoise blue and phenol). In each experiment, 50 ml aqueous solution containing of 0.2 mM of dye and 50 mg of catalyst was added in reaction cell. The reactant solution was tightly closed and stirred in dark for 20 min to attain the homogenous suspension and adsorption/desorption of dye on catalyst surface. Then whole set up was placed under sunlight and stirred vigorously for 6 hrs at room temperature. At regular interval of 1 hour, about 5 mL of suspension was withdrawn, centrifuged at 6000 rpm for 30 min and analyzed by UV/Visible Spectrophotometer.

3. Result and discussions

3.1. Characterization of SiO_2-TiO_2 nanocomposite

3.1.1. X-Ray diffraction studies

Table 1. Particle Size, EDX and RBS data of prepared SiO_2-TiO_2 nanocomposites.

No	Catalyst	Particle size (nm)	EDX (Atomic percent)		RBS (Atomic percent)	
			TiO_2	SiO_2	TiO_2	SiO_2
1	20% SiO_2·TiO_2	28	82.86	17.1	80.16	19.84
2	30% SiO_2·TiO_2	25	71.53	29.3	69.23	30.77
3	40% SiO_2·TiO_2	20	61.10	38.9	59.51	40.49
4	50% SiO_2·TiO_2	18	48.00	52.0	51.25	48.75

XRD patterns of synthesized nanocomposite with varying SiO_2 contents (20%, 30%, 40% and 50%), calcined at 550 °C are presented in Figure 1. XRD patterns of all samples and the corresponding characteristic 2θ values of the diffraction peaks confirmed the anatase-phase of TiO_2 (ICDD PDF 21-1272). The gradually decrease in peak intensity and broadening of diffraction peaks with increasing silica contents suggests a decreasing long-range order due to aggregation of amorphous silica on TiO_2 surface thus lowering content of TiO_2 particles [25,26] and it is consistent with the following SEM. Moreover, no phase transformation from anatase to rutile observed upon addition of SiO_2 [20]. The average crystalline size of nanocomposite was estimated from the peak half-width B, using Scherrer's equation [21] and tabulated in Table 1.
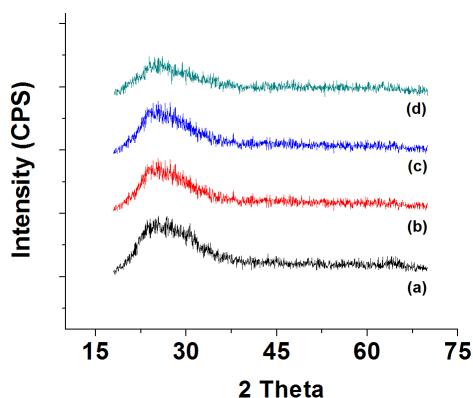
Figure 1. XRD patterns of (a) 20% SiO_2-TiO_2 (b) 30% SiO_2-TiO_2 (c) 40% SiO_2-TiO_2 and (d) 50% SiO_2-TiO_2 nanocomposite.

3.1.2. Scanning electron microscopy (SEM)

Figure 2a-d exhibits SEM micrographs corresponding to SiO_2-TiO_2 nanocomposite with different wt % of SiO_2 (20 wt%, 30 wt%, 40 wt% and 50 wt %). It evident from micrographs that nanocomposites with 20% SiO_2 composed of individual TiO_2 and SiO_2 particles (of around 20 nm size) and some aggregates (of 30-40 nm size). Whereas the micrographs with high silica contents demonstrate titania particles embedded in a dense silica matrix. Furthermore, SEM micrographs also provide evidence that nanocomposite consist of mesoporous aggregates and amount of agglomeration increased with addition of silica contents owing to the aggregation of amorphous silica on TiO_2 surface. These observations are consistent with our XRD results. Similar pattern of titania-silica nanocomposite have also obtained by Luis *et al.* and Natalia *et al.* [28,29]. Energy dispersive X-Ray analysis was carried for the determination of elemental composition of the prepared SiO_2-TiO_2 nanocomposite (shown in Table 1), which is consistent to theoretical calculations.

3.1.3. Rutherford back scattering spectroscopy (RBS)

Figure 3 shows the combined RBS experimental spectra of the all nanocomposites. The composition profile analysis of the SiO_2-TiO_2 nanocomposite is summarized in Table 1. RBS depth profile data of all samples clearly depicts the presence of

homogenous single layer, which strongly suggests that SiO_2 nanoparticles are practically well and homogenously distributed on surface of titania particle [30,31]. Moreover, these elemental compositions determine by RBS are consistent to those determined by EDX and summarized in Table 1.
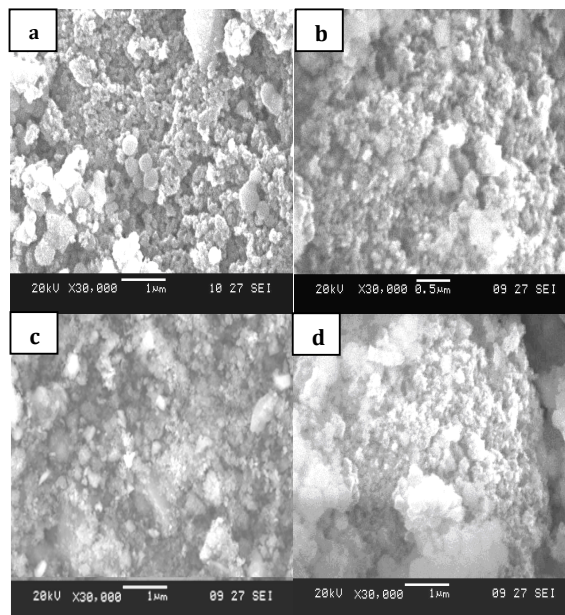
Figure 2. SEM micrographs of (a) 20% SiO_2-TiO_2 (b) 30% SiO_2-TiO_2 (c) 40% SiO_2-TiO_2 and (d) 50% SiO_2-TiO_2 nanocomposite.
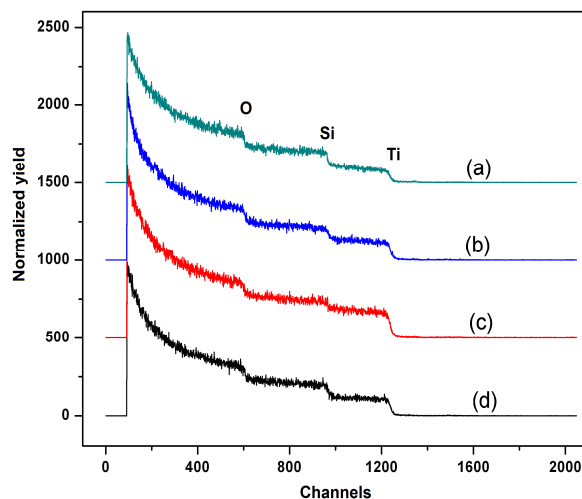
Figure 3. RBS spectra of (a) 20% SiO_2-TiO_2 (b) 30% SiO_2-TiO_2 (c) 40% SiO_2-TiO_2 and (d) 50% SiO_2-TiO_2 nanocomposite.

3.1.4. Thermal analysis

The thermal stability of titania nanoparticles is one of the significant constraints for its use as catalyst support. To

investigate the thermal stability SiO_2-TiO_2 nanocomposites TGA analysis was conducted up to 1000 °C with an interval of 10 °C as shown in Figure 4. All samples exhibited somehow similar pattern of thermal behavior with three step weight loss. First weight loss appeared in the range of 150-200 °C can be attributed to the evaporation of adsorbed water and thermal decomposition of the isopropanol [26]. The second weight loss appeared in the range of 350 to 500 °C may be due to the decomposition of the surfactant and water molecules formed from condensation of hydroxyl groups on the particle's surface (TiOH) [27,28]. Notably, above 600 °C no weight loss observed depicting that the nanocomposites are stable and free of any organic contaminants, while minor weight change appeared at high temperatures may be due to de-hydroxylation. The total mass loss of SiO_2-TiO_2 nanocomposites was 13%, 17%, 20% and 25% for 20% SiO_2-TiO_2, 30% SiO_2-TiO_2, 40% SiO_2-TiO_2 and 50% SiO_2-TiO_2 nanocomposite, respectively. As it is found that the weight loss increased with the addition of SiO_2 which correspond to the increased amount of organic compounds and hydroxyl groups with increase in silica contents [30]. The materials calcined in air are organic residue free and have reasonable stability after 600 °C. On the basis of these results the calcination temperature for SiO_2-TiO_2 nanocomposites was selected at 550 °C in order to obtain the anatase-TiO_2.
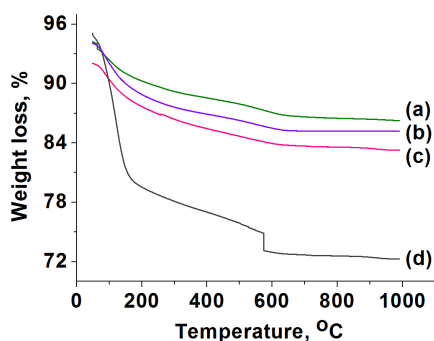
Figure 4. TGA analysis of (a) 20% SiO_2-TiO_2 (b) 30% SiO_2-TiO_2 (c) 40% SiO_2-TiO_2 and (d) 50% SiO_2-TiO_2 nanocomposite.

3.1.5. Fourier transform infrared spectroscopy (FTIR)

Comparative FT-IR spectra of the prepared nanocomposites are shown in Figure 5. All samples present the typical silica bands. Particularly, the peaks located at 800 and 1050 cm^{-1} are representative of Si-O-Si bending and stretching vibration [31]. Related to the titania bands, it is mentioned earlier that bands observed in the region of 900-1000 cm^{-1} may be associated to stretching vibration of Ti-OH and Ti-O-Si species [28,30]. These bands appear due to co-condensation between titania and silica nanoparticles within composite. Though, these bands are not enough strong and prominent in our spectra because they are obscured by the Si-OH peaks located in the same region. Specifically, the band at 1280 cm^{-1} is attributed to stretching vibrations of C-H bonds [30-32]. Finally, the broad bands appearing at 3400 cm^{-1} and 1620 cm^{-1} correspond to stretching vibrations of O-H bonds with absorbed molecular water. It is obvious from the spectra that absorption intensity near 3400 and 1620 cm^{-1} increased with increasing silica contents due to capability of silica to adsorb water [28,33].

3.1.6. Diffuse reflectance spectroscopic analysis

The band gap energies were determined from UV-visible diffuse reflectance spectrum. The comparative UV-visible diffuse reflectance spectrum of SiO_2-TiO_2 nanocomposites recorded in the range of 200-800 nm at room temperature is shown in Figure 6. It is obvious from the Figure 6 that the

absorption bands changed significantly with addition of SiO_2 and thus resulting in change in band gap energy. The addition of 20% SiO_2 to TiO_2 shifted the band from 415 nm to 600 nm thus inducing larger red shift towards visible region while further addition of SiO_2 from 20% to 50%, characteristic blue shift was observed towards UV region. The optical band gap energy of the nanocomposites was evaluated from the reflectance data of the nanocomposites obtained from DRS technique. The reflectance data in term of Kubelka-Munk function was estimated using the equation (1) [29,30].

$$F(R) = (1-R)^2/2R \qquad (1)$$

where F(R) and R represent the Kubelka-Munk function and absolute value of reflectance, respectively. The band gap energies of the SiO_2-TiO_2 nanocomposite can be derived by Tauc plot [28] which is obtained by plotting $(F(R)*h\nu)^2$ vs energy (eV). The band gaps of these nanocomposites were calculated by extrapolation of linear region of the plot to the energy axis (Figure 7). The comparative band gap energy values of all samples are given in Table 2, the band gap energies clearly reveal that addition of 20%-SiO_2 to TiO_2 resulted in decrease in optical band gap energy from 3.2 to 2.95 eV as compared with mesoporous TiO_2 suggesting the structural interruption in the titania framework due to addition of SiO_2. However, the band gape energies of SiO_2-TiO_2 nanocomposites significantly increased from 2.95 to 3.2 eV as the amount of SiO_2 increased from 20% to 50%, implying that TiO_2 nanoparticles are pierced inside silica matrix resulting in reduction in anatase TiO_2 availability on the surface of nanocomposite [30,34,35]. These findings are in well agreement with the observed photocatalytic activity.
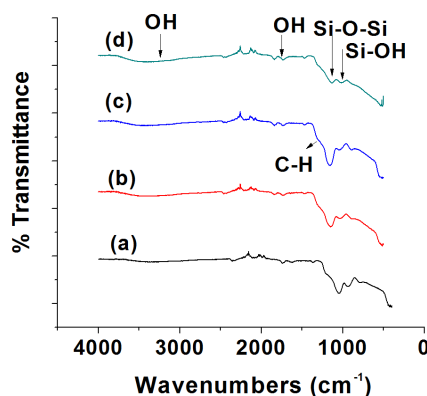
Figure 5. FT-IR patterns of a) 20% SiO_2-TiO_2 (b) 30% SiO_2-TiO_2 (c) 40% SiO_2-TiO_2 and (d) 50% SiO_2-TiO_2 nanocomposite.
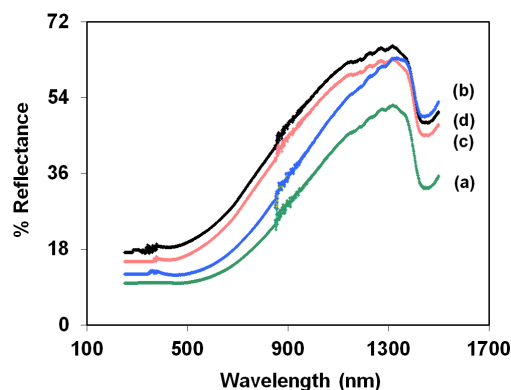
Figure 6. Diffuse reflectance patterns of a) 20% SiO_2-TiO_2 (b) 30% SiO_2-TiO_2 (c) 40% SiO_2-TiO_2 and (d) 50% SiO_2-TiO_2 nanocomposite.

Table 2. Textural Parameters of prepared SiO_2-TiO_2 nanocomposites.

No	Catalyst	Band gap energy (eV)	BET surface area (m^2g^{-1})	Pore size (nm)	Pore volume (cc/g)
1	20% SiO_2.TiO_2	2.95	319.58	13.09	2.44
2	30% SiO_2.TiO_2	3.00	357.90	12.42	2.38
3	40% SiO_2.TiO_2	3.10	399.68	11.75	1.89
4	50% SiO_2.TiO_2	3.20	411.55	102.83	1.28
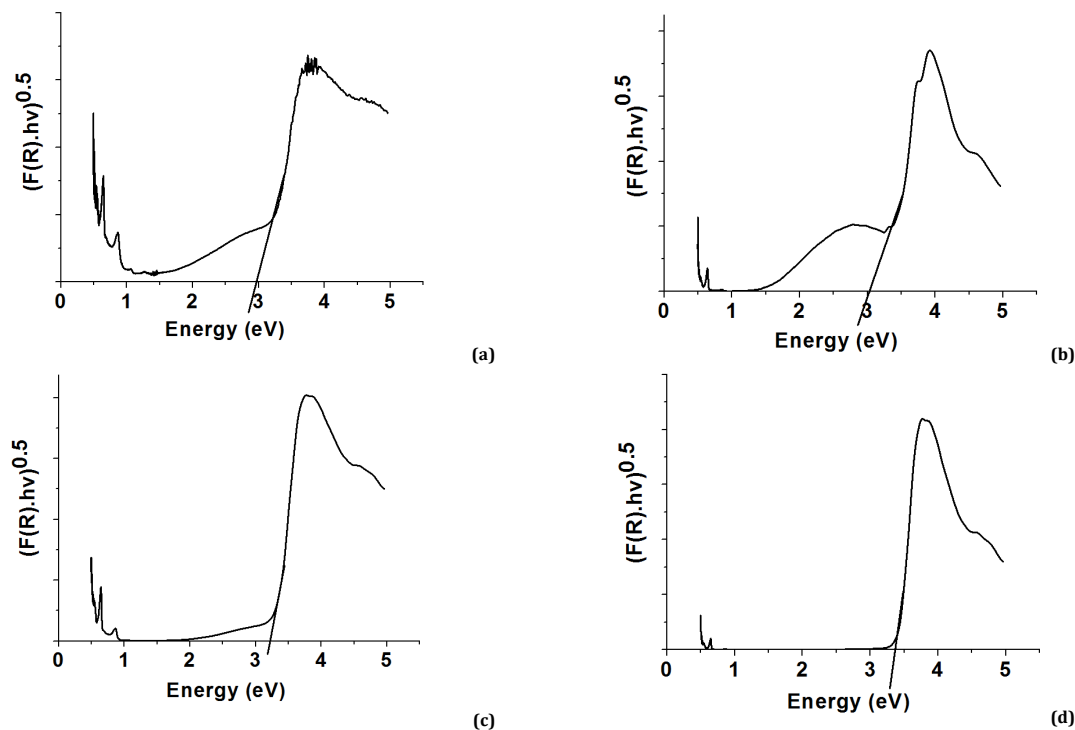
Figure 7. Diffuse reflectance patterns of a) 20% SiO_2-TiO_2 (b) 30% SiO_2-TiO_2 (c) 40% SiO_2-TiO_2 and (d) 50% SiO_2-TiO_2 nanocomposite.

3.1.7. BET instrument analysis

The textural parameters including BET surface area, pore volume and pore diameters of the nanocomposites are summarized in Table 2. It is observed that the material with high silica contents, specific surface of mesoporous silica-titania nanocomposites is high while the pore volume and pore diameter is appreciably small. Notably, the specific surface area of TiO_2 with 50% SiO_2 (411.55 m^2/g) is considerably higher than 20% SiO_2-TiO_2 (319.58 m^2/g) nanocomposite. Concerning the effect of silica on the pore size and pore volume, it is observed that 20% SiO_2-TiO_2 has appreciably high pore volume as well as pore diameter than 50% SiO_2-TiO_2 (as shown in Table 2). The increase in surface area upon addition of SiO_2 to TiO_2 is in agreement with reduction in grain size (as discussed in XRD) [29,31]. The low pore volume and pore size at high silica contents can be attributed to the agglomerates of titania particle intercalated in the intrapartilce spaces and interparticle voids formed between silica particles which lowers the availability of titania on the surface of nanocomposites [32,34]. It can be speculated from these findings that large pore volume and pore diameter resulted in mesoporous composite with high adsorption/desorption capacity and eventually excellent photocatalytic activity [35].

3.2. Photocatalytic activity measurements of SiO_2-TiO_2 nanocomposite

The photocatalytic activity of SiO_2-TiO_2 nanocomposite was assessed by photocatalytic degradation of methyl yellow, auramine O, turquoise blue G and phenol under visible irradiations. The degradation rates were studied at interval of one hour by the change in concentration of dyes and phenol through UV-visible spectroscopy. The percent degradation rate of dyes and phenol with reaction time was computed by using Equation (2) [26,27].

$$X= (C_o-C)/C_o \times 100 \qquad (2)$$

where C, C_o and X is initial concentration, concentration at time "t" and degree of photodegradation, respectively. The results obtained for percent degradation and comparison of photocatalytic degradation of dyes and phenol with different SiO_2-TiO_2 nanocomposites are represented in Figure 8a-d. It is obvious from the results that concentration of dyes and phenol decreased with time for all nanocomposites. Initially the decomposition of dyes and phenol was negligible with all nanocomposites although the rate of degradation increased with time and maximum degradation was attained after 6hrs. In addition, the photocatalytic activity declined also with increase in SiO_2 concentration, it is noteworthy from the figure 8 that activity of 20% SiO_2-TiO_2 with all dyes and phenol is remarkably higher than that of TiO_2 with high silica contents which decreased progressively with increase in SiO_2 concentration. The maximum conversion achieved by 20% SiO_2-TiO_2 nanocomposites was 86% for auramine O, 78.9% for methyl yellow, 73.7% for phenol and 59.8% for direct turquoise after 6 hrs as shown in Figure 8. However, the excellent photocatalytic activity of 20% SiO_2-TiO_2 nanocomposite can be accomplished to high pore volume and pore diameter, more surface hydroxyl groups, high crystallanity of anatase nanocomposite and small band gap energy [33].

Table 3. Comparison of the rate constants of auramine, methyl yellow, phenol and turquoise blue with SiO_2-TiO_2 nanocomposite at room temperature.

Catalyst	Rate constants , K (s^{-1})			
	Phenol	Auramine O	Methyl Yellow	Direct Turquoise
20% SiO_2 -TiO_2	0.0039	0.0052	0.0037	0.0023
30% SiO_2 -TiO_2	0.0031	0.0042	0.0029	0.0013
40% SiO_2 -TiO_2	0.0021	0.0031	0.0024	0.0008
50% SiO_2 -TiO_2	0.0019	0.0023	0.002	0.0004
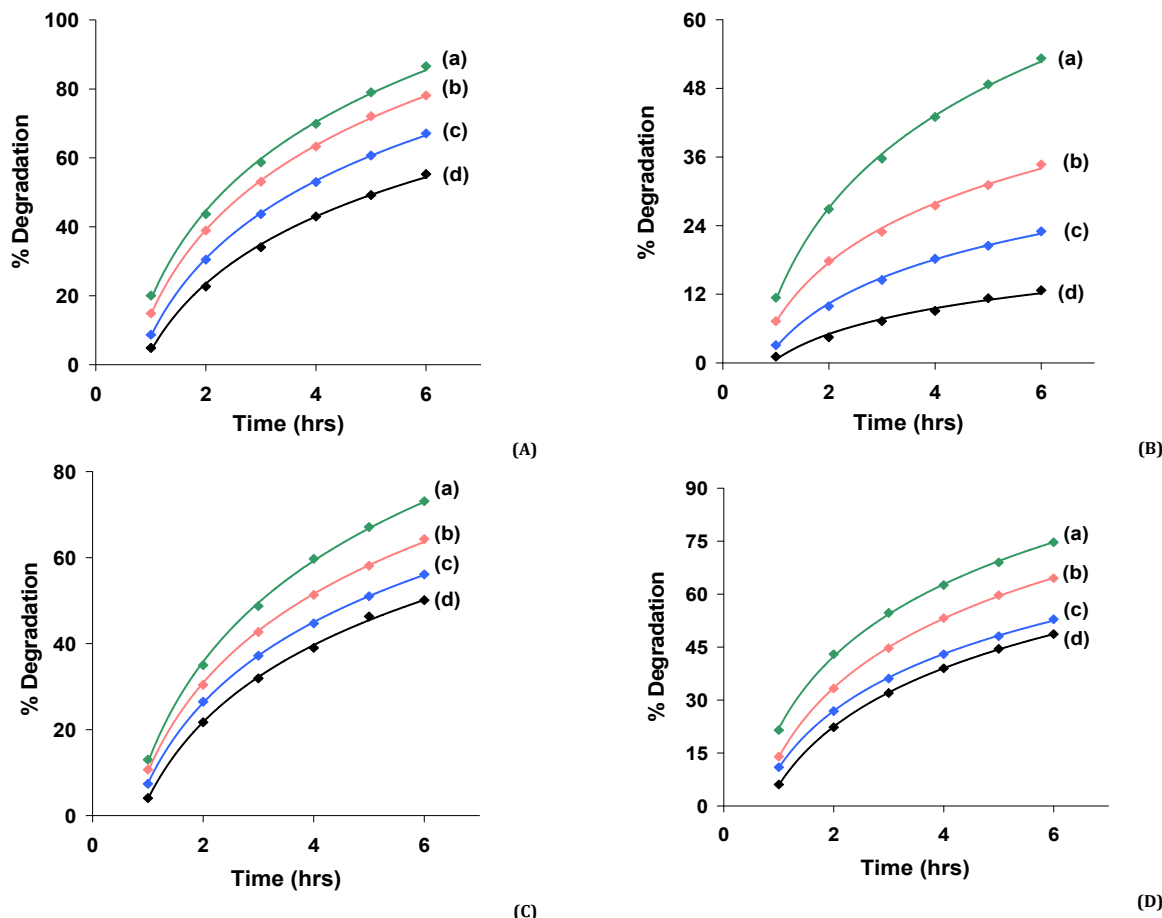
Figure 8. Percent degradation of (A) auramine (B) methyl yellow, (C) phenol and (D) turquoise blue on SiO_2-TiO_2 nanocomposite where, a) 20% SiO_2-TiO_2 (b) 30% SiO_2-TiO_2 (c) 40% SiO_2-TiO_2 and (d) 50% SiO_2-TiO_2 nanocomposite.

Furthermore, photocatalytic activities are fully contrary to the surface area of nanocomposites depicting non-correlativity between surface area and photocalytic activity. The decline in catalytic activity at high silica concentration is due to the fact that excessive addition of SiO_2 reduces the availability of anatase TiO_2 by covering the active sites of TiO_2 [35].

3.3. Kinetics of catalytic reaction

Adsorption kinetics is one of crucial factor which can be used not only to compare the catalytic activity of different nanocomposites but also it illustrates the relationship between photocatalytic degradation and adsorption behavior of dyes on catalyst surface. It is found that adsorption of dye on the catalyst surface follows the pseudo first order kinetics, Equation (1) depicts the simplified pseudo-first-order kinetics equation [29,34,35].

$$Ln (C_o/C) = k_{ads}.t \tag{3}$$

where k_{ads} is the apparent pseudo-first-order rate constant (1/min), C_o is the initial concentration (mg/L) and C is

concentration (mg/L) at time "t". Generally, a logarithmic plot of concentration versus time gives a straight line with slope equal to pseudo-first-order rate constant (k_{ads}).

The effect of SiO_2 contents on the photocatalytic activity of SiO_2-TiO_2 nanocomposites in degradation of dyes and phenol is given in Figure 9 and calculated values of k_{ads} for catalytic reaction of all nanocomposites are summarized in Table 3.

Higher is the value of k_{ads}, higher will be the adsorption capacity and degradation of reactants and ultimately greater will be the catalytic activity of nanocomposites. It can be seen from Figure 9 and Table 3 that all dyes have different value of k_{ads} showing different adsorption capability and different degradation rates of dyes on the catalyst surface. It is obvious from the results summarized in Table 3, which value of k_{ads} increased with increase in SiO_2 amount up to 20% which depicts the strong adsorption of dye on SiO_2-TiO_2 nanocomposite surface and high photocalaytic activity. But value of k_{ads} decreased when the amount of silica increased above 20%, showing decrease in photocatalytic degradation. This behavior can be attributed to high pore volume, pore diameter, small band gap energy and high availability of anatase TiO_2 for 20% SiO_2-TiO_2 nanocomposite.
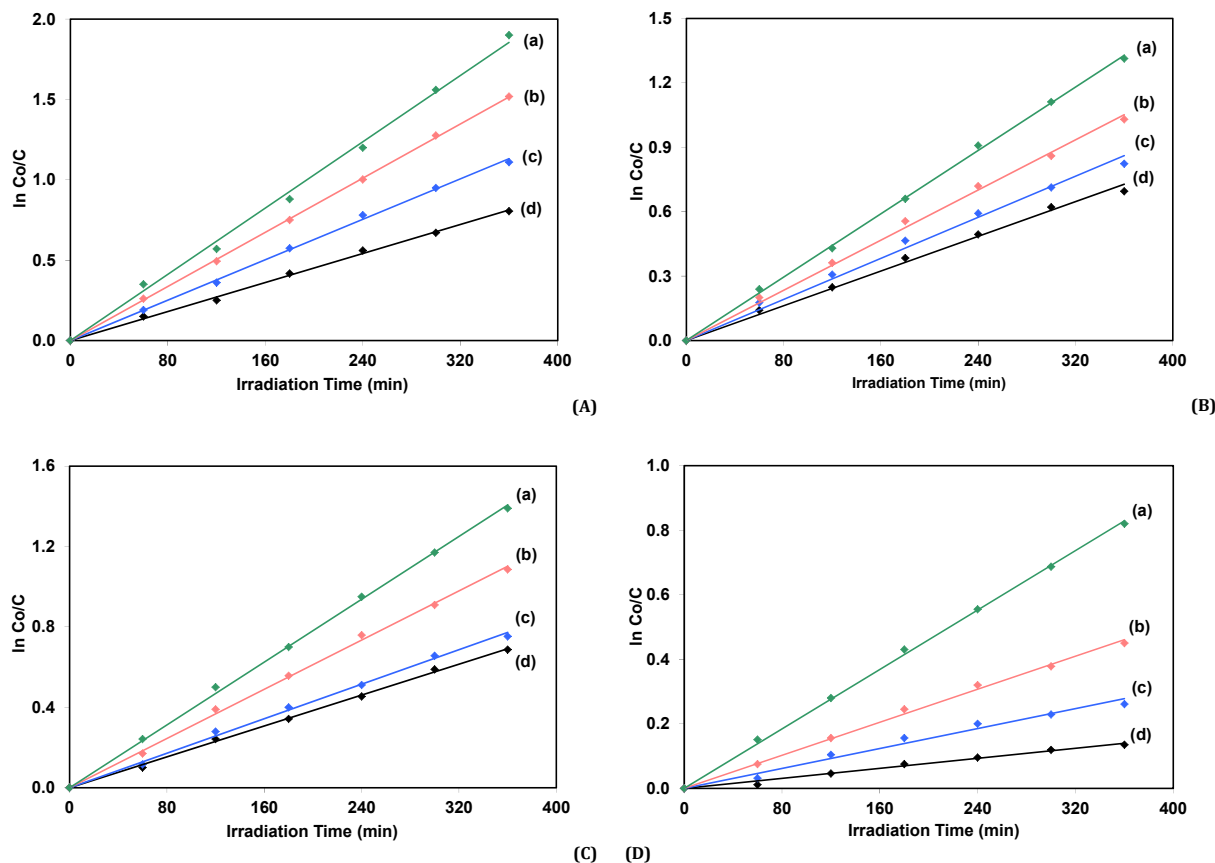
Figure 9. Kinetics of adsorption of (A) auramine (B) methyl yellow, (C) phenol and (D) turquoise blue on SiO_2-TiO_2 nanocomposite where, a) 20% SiO_2-TiO_2 (b) 30% SiO_2-TiO_2 (c) 40% SiO_2-TiO_2 and (d) 50% SiO_2-TiO_2 nanocomposite.

Notably, large pore volume and pore diameter facilitates the mass transfer of reactants consequently resulting in maximum adsorption and degradation, as depicted by high value of k_{ads} in case of 20% SiO_2-TiO_2 nanocomposite. Furthermore, kinetic data given in Table 3 also suggests that adsorption rate constants for auramine O, methyl yellow and phenol is significantly high as compared to direct turquoise for 20% SiO_2-TiO_2 nanocomposite. This can be attributed to complex molecular structure of direct turquoise due to which its probability of adsorption deceases on catalyst surface and hence catalytic activity reduces [35]. From these findings, it can be accomplished that high pore volume, pore diameter and reduced bandgap imparts crucial role in the photocatalytic activity.

4. Conclusions

a) Mesoporous silica-titania composites with varying SiO_2-TiO_2 ratio have been fabricated successfully by an effective and facile micro emulsion method. The implication of present synthesis method relies in its simplicity, high yield with high porosity, surface area and low band gap energy.
b) The photocatalytic performance of mesoporous nanocomposites was demonstrated for photocataytic degradation of dyes and phenol under visible irradiation with different interval of time.
c) Furthermore, the effect of SiO_2 contents on the photocatlytic activity was also examined and compared in terms of percent degradation and kinetic parameters.
d) Among all nanocomposites, 20% SiO_2-TiO_2 based nanocomposite exhibited excellent catalytic performance

owing to its low band gap energy, high pore volume and pore diameter and high availability of anatase TiO_2 nanocrystals.
e) It can be concluded from the findings that SiO_2-TiO_2 based nanocomposites depict profound potential for photocatalytic degradation of environmental hazardous substances from contaminated water.

References

[1].   Montgomery, M. A.; Elimelech, M. *Envir. Sci. Tech.* **2007**, *41*, 17-24.
[2].   Singh, P.; Bengtson, L. *J. Hydrol.* **2005**, *300*, 140-154.
[3].   Richardson, S. *Anal. Chem.* **2003**, *75*, 2831-2857.
[4].   Kyung, H.; Lee J.; Choi, W. *Envir. Sci. Tech.* **2005**, *39*, 2376-2382.
[5].   Li, X. *J. Phys. Chem. C* **2007**, *111,* 13109-13116.
[6].   Weiyang, D.; Chul, W. L.; Xinchun, L.; Yaojun, S.; Weiming, H.; Guoshun, Z.; Shicheng, Z.; Jianmin, C.; Huiqi, H.; Dongyuan, Z. App. *Catal. B-Environ.* **2010**, *95*, 197-200.
[7].   Weber, E. J.; Adams, R. L. *Envir. Sci. Tech.* **1995**, *29*, 1163-1165.
[8].   Jung, K. Y.; Park, S. B. *Chem. Eng. J.* **2001**, *18*, 879-888.
[9].   Ollis, D. F. *Envir. Sci. Tech.* **1985**, *19*, 480-486.
[10]. Benkli, Y. E.; Can, M. F.; Turan, M.; Celik, M. S. *Water Resour.* **2005**, *39,* 487-493.
[11]. Selcuk, H. *Dyes Pigments* **2005**, *64*, 217-222.
[12]. Ghoreishi, S. M.; Haghighi, R. *Chem. Eng. J.* **2003**, 95163-95169.
[13]. Legrini, O.; Oliveros, E.; Braun, A. M. *Chem. Rev.* **1993**, *93*, 671-698.
[14]. Vandevivere, P. C.; Bianchi, R. Verstraete, W. *J. Chem. Technol. Biot.* **1998**, *72*, 289-302.

[15]. Neelavannan, M. G.; Revathi, M.; Basha, C. A. *J. Hazard. Mater.* **2007**, 149, 371-378.

[16]. Hussain, S. T.; Siddiqa, A.; Ilyas, H.; Muhammad, B. *Int. Rev. Chem. Eng. Rapid Commun. (IRECHE).* **2012**, *4,* 547-553.

[17]. Lalov, I. G.; Guerginov, I. I.; Krysteva, M. A.; Fartsov, K. *Water Resour.* **2000**, *34,* 1503-1506.

[18]. Gogate, R.; Pandit, A. B. *Adv. Environ. Res.* **2004**, *8,* 501-551.

[19]. Chen, D.; Ray, A. K. *Chem. Eng. Sci.* **2001**, *56,* 1561-1570.

[20]. Zhao, C.; Chen, Y.; Wang, W.; Ma, J.; Zhao, T. Rajh, L. *Envir. Sci. Tech.* **2008**, *42,* 308-314.

[21]. Xu, Y.; Langford, C. H. *J. Phys. Chem. C* **1995**, *99,* 11501-11507.

[22]. Habibi, A.; Hassan, S. M. *J. Photoch. Photobio. A: Chem.* **2005**, *172,* 89-96.

[23]. Tada, H.; Kubo, Y.; Akazawa, M. *Languir* **1998**, *14,* 2936-2939.

[24]. Chih-Hung, H.; Kai-Ping, C.; Hong-De, O.; Yu-Chun, C.; Chang, E.; Chu-Fang, W. *J. Hazar. Mater.* **2011**, *186,* 1174-1182.

[25]. Xingtao, G.; Israel, E. *Catal. Today* **1999**, *51,* 233-254.

[26]. Yuying, P. U.; Fang, J.; Feng, P.; Baojian, L. I.; Lei, H. *Chinese J. Catal.* **2007**, *28,* 251-256.

[27]. Ali, M.; Mohammad, A. B.; Naser, M. *Photochem. Photobiol.* **2011**, *87,* 795-801.

[28]. Luis, P.; Maria, J. M. *j. Phys. Chem. C* **2011**, *15,* 22851-22862.

[29]. Natalia, N. T.; Alexander, A. P.; Emil, R. *Langmuir* **2005**, *21,* 10545-10554.

[30]. Zhe-Ying, S.; Long-Yu, L.; Yat, L.; Chang-Chun, W. *J. Colloid. Interf. Sci.* **2011**, *354,* 196-201.

[31]. Hussain, S. T.; Siddiqa, A. *Int. J. Environ. Sci. Te.* **2011**, *8,* 351-362.

[32]. Hu, C.; Wang, Y.; Tang, H. *Appl. Catal. B: Environ.* **2001**, *35,* 95-105.

[33]. Lee, J. W.; Othman, M. R.; Eom, Y.; Lee, T. G.; Kim, W. S.; Kim, *J. Appl. Catal. B: Environ.* **2001**, *35,* 95-105.

[34]. Dina, F. R.; Johann, M. S.; Qianqian, Y.; Vit, K.; Jiri, R.; Thomas, B. *Chem. Mater.* **2009**, *21,* 2410-2417.

[35]. Carl, A.; Allen, J. B. *J. Phys. Chem. B* **1997**, 101, 2611-2616.